coatings

MDPI

Article

Laser Preparation and Underwater Drag-Reduction Performance of Secondary Fractal–V Groove Composite Structures on the Surface of Equal-Diameter Revolution Bodies

Yan Wang [1,2,3], Zhanpeng Hu [1,2], Qian Zhang [1,2], Zhisheng Yang [1,2], Xueyan Zhao [1,2] and Yonghua Wang [1,2,*]

[1] Ministry of Education Key Laboratory for Cross-Scale Micro and Nano Manufacturing, Changchun University of Science and Technology, Changchun 130022, China; wangyan@cust.edu.cn (Y.W.); huzhan1129@163.com (Z.H.); zqian1115@163.com (Q.Z.); fallowesxloruyt@gmail.com (Z.Y.); 18186890524@163.com (X.Z.)
[2] College of Mechanical and Electrical Engineering, Changchun University of Science and Technology, Changchun 130022, China
[3] School of Mechanical and Aerospace Engineering, Jilin University, Changchun 130025, China
* Correspondence: 45050524@163.com

Abstract: The reduction of drag for both aircraft and underwater equipment has the potential to reduce their overall energy consumption. Consequently, research into the drag-reducing performance of metal surfaces has significant practical applications. However, there has been more research on the machining of grooves on flat surfaces and inside tubes and less research on the structure of drag-reducing grooves on the outside of circular rods. This paper presents a study in which laser etching technology is employed to machine a range of secondary fractal topologies and V-groove composite structures on the surface of equal-diameter stainless-steel bodies of revolution. The influence of different parameters on the surface properties of stainless-steel materials is analysed through the use of auxiliary positioning tools, adjustments to laser processing parameters and scanning path schemes, as well as the characterisation of the surface morphology of the processed stainless steel using super-depth microscopy, scanning electron microscopy, and other techniques. Subsequently, an underwater drag-reduction tester is employed to assess the drag-reduction efficacy of the optimised secondary fractal composite structure on the surface of the stainless-steel equal-diameter body of revolution. Subsequently, particle image velocity (PIV) tracking technology is employed to assess the surface flow field velocity and overall velocity average of the secondary fractal composite structure. The findings indicate that the secondary fractal composite structure exhibited a drag-reduction effect on the surface of the stainless-steel body of revolution only when the primary main groove had a width of 0.1 mm. Furthermore, an increase in the Reynolds number Re within the range of 4000 to 7000 resulted in a notable enhancement in the drag-reduction efficacy of the secondary fractal composite structure on the surface of the stainless-steel body of revolution. At Re values of 5000, 6000, and 7000, the corresponding drag-reduction rates were observed to be 5.15%, 5.28%, and 5.40%, respectively.

Keywords: secondary fractal; composite structure; laser processing; equal diameter body of revolution; underwater drag reduction

check for updates

Citation: Wang, Y.; Hu, Z.; Zhang, Q.; Yang, Z.; Zhao, X.; Wang, Y. Laser Preparation and Underwater Drag-Reduction Performance of Secondary Fractal–V Groove Composite Structures on the Surface of Equal-Diameter Revolution Bodies. *Coatings* **2024**, *14*, 1613. https://doi.org/10.3390/coatings14121613

Received: 22 November 2024
Revised: 18 December 2024
Accepted: 19 December 2024
Published: 23 December 2024

Copyright: © 2024 by the authors. Licensee MDPI, Basel, Switzerland. This article is an open access article distributed under the terms and conditions of the Creative Commons Attribution (CC BY) license (https://creativecommons.org/licenses/by/4.0/).

1. Instruction

As a consequence of the accelerated growth of maritime military and marine resources, there has been a concomitant expansion in the scope of human exploration of the ocean, extending to the deep sea and the open sea. It is therefore of great significance to reduce the cruise drag of the hull and the resistance of the equipment when working in the water, with the aim of reducing energy consumption and prolonging the voyage range and effective working time [1]. Prior to the 1960s, the prevailing scientific opinion was that a surface with

minimal irregularities would result in the lowest possible flow resistance when submerged. The objective of research into surface drag-reduction technology has consistently been the reduction of surface roughness and the attainment of a sufficiently smooth surface. A more detailed examination of the microstructure of the surface of objects revealed that a surface with a specific texture structure exhibited an enhanced underwater drag-reduction effect. In the 1960s, NASA Langley Research Center made the discovery that a rib structure (with tiny downstream grooves on the surface) can reduce the frictional resistance of the wall surface [2]. This marked the first instance of a challenge to the long-held belief that a surface with a smoother texture would inherently exhibit lower friction resistance. Additionally, the research team identified that V-grooves of a specific scale were the most effective geometry for reducing drag. The advancement of turbulence theory [3–5], particularly the development of experimental techniques and numerical simulation calculations [6–9], has provided a theoretical foundation for trench drag-reduction technology, which has subsequently been applied in practice [10–13].

Despite the existence of numerous studies examining the efficacy of groove-based drag-reduction techniques on metal surfaces, the majority of these studies have concentrated on flat metal surfaces, with relatively limited research exploring the potential of groove-based drag reduction on curved surfaces. The majority of research on the use of grooves to reduce drag on curved surfaces has been conducted on the inner surface of circular pipes. Conversely, there is a paucity of research on the design and processing ofdrag-reduction structures on the outer surface of circular rods or bars. Nitschke et al. [14] conducted an analysis of the resistance and flow field on the surface of a groove structure inside a circular tube. Their findings indicate that when the groove valleys and peaks are flat and the groove spacing s_+ falls within the range of 8–25, the groove surface inside the circular tube is capable of achieving a drag-reduction function. Subsequently, further research has revealed that the drag-reduction rate can reach up to 3% when s_+ is within the range of 11–15. Nevertheless, some scholars have conducted research on this basis and applied this structure to the outer surface of a circular tube. Their findings indicate that the size and shape of the groove are not the optimal combination for achieving the bestdrag-reduction effect. Rapp et al. [15] modified the groove shape based on Nitschke's findings and discovered that thedrag-reduction performance of rectangular groove surfaces is closely associated with groove size. Auteri F et al. [16] conducted research and analysis on the travelling wave wall and found that the drag-reduction rate of the groove surface inside the pipeline can reach 33%. In a study conducted by Fei Tang et al. [17], the effectiveness of a travelling wave wall surface in reducing drag was investigated using AuteriF. The results demonstrated that the surface exhibited a favourable drag-reduction effect when moving in a forward direction. Yulia et al. [18] conducted a simulation analysis of the surface resistance and flow field of triangular grooves under both parallel and sinusoidal flow conditions. The findings indicated that the drag-reduction rate of sinusoidal groove surfaces was significantly higher than that of parallel triangular groove surfaces. Dengke Chen et al. [19] drew inspiration from the tooth-like structure of shark skin and proposed a drag-reduction method for adaptive underwater vehicles with complex curved surfaces. This involved adjusting the surface groove structure parameters of deformable flexible vehicles.

In these studies, common grooves include single-section through-groove structures and complex biomimetic groove structures. The processing of through-groove structures is simple, but their ability to reduce drag is limited, while the complex processing of biomimetic groove structures is difficult, especially in achieving large-area precision manufacturing [20]. In nature, a large number of organisms have their own unique survival skills, and there are many natural structures with similar tree-net structures, such as the blood circulation system and the respiratory system in animals, the water and nutrient transport system in plant trunks and veins, and the distribution system of river tributaries. This structure is a relatively optimised structure selected by natural selection, with advantages such as low flow resistance, low energy loss, and high energy exchange rate [21,22]. Benoit B. Mandelbrot, a mathematics professor at Harvard University in the United States,

proposed the concept of self-phase fractals as early as 1975 [23]. His first book on self-phase fractals, "Fractal, From, Chance, and Dimension", inspired people to draw ideas from the disordered or mixed surface structures in nature in order to obtain various correlations between the internally ordered and overall structures of these surface structures. Therefore, we simplified the structure of leaf veins and other structures, obtained a secondary fractal structure, and used the fractal structure as the topology of the V-shaped groove. On the basis of increasing the drag-reduction ability of the through-groove structure, we reduced the processing difficulty.

At the present time, there are a plethora of processing techniques for the reduction of groove drag on surfaces. The most common processing methods for surface groove structures are lithography [8,24,25], 3D printing [26], laser ablation [9,27,28], mechanical processing [29–31], and direct replication [32,33]. The materials that can be processed by these methods exhibit a range of processing accuracy, manufacturing efficiency, and processing cost, with each method offering a distinct set of advantages and disadvantages. Laser ablation, as a non-contact machining method, does not suffer from the issue of tool wear and the heat-affected zone is relatively limited. Furthermore, the utilisation of a laser as the machining medium exhibits the attributes of high precision, high efficiency, and robust controllability, enabling the effective processing of drag-reducing groove structures on diverse material surfaces. In particular, lasers can be used to process groove structures on various material surfaces and to improve their tribological and adhesive properties [34,35]. Nevertheless, the majority of studies examining the use of lasers for drag-reduction groove machining are conducted on flat substrates, with the actual workpieces typically comprising curved surfaces. Consequently, the efficient and precise machining of curved surface structures represents a significant challenge in the laser processing of surface grooves.

This study proposes a simple secondary fractal composite drag-reduction structure by combining a secondary fractal structure with V-shaped grooves. Using positioning tools, the structure is prepared on the surface of the equal-diameter body of revolution of 304 stainless steel by laser etching. Based on the principles and characteristics of laser processing, the laser processing parameters and scanning path scheme are changed to optimise the shape and size of the V-shaped groove, thus achieving the optimal laser processing technology for equal-diameter body of revolution surfaces, as shown in Figure 1. The surface morphology of the processed stainless-steel is characterised by ultra-depth microscopy, scanning electron microscopy, etc., and the influence of various parameters on the surface properties of stainless-steel materials is analysed. Finally, the PIV particle-tracking velocimetry technique was used in conjunction with a cyclic channel drag-reduction test bench to test the drag-reduction performance of the simulated leaf-vein structure surface and to analyse the drag-reduction mechanism of the secondary fractal composite structure.

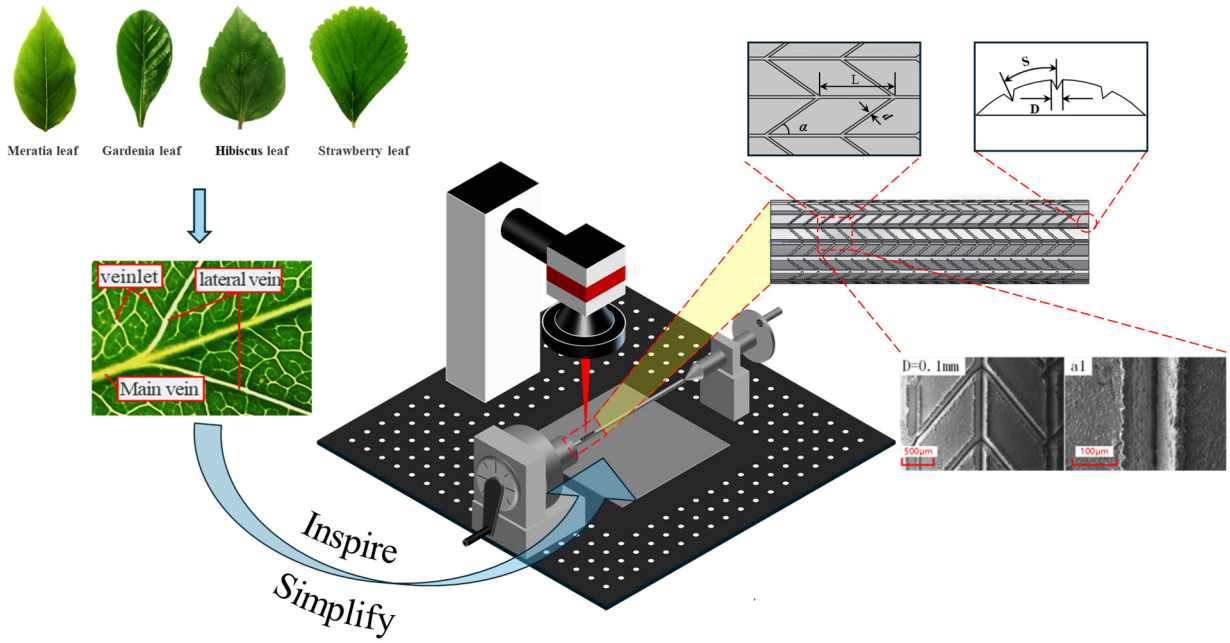


Figure 1. Laser processing of secondary fractal composite drag-reduction structure of stainless-steel equal-diameter body of revolution.

2. Materials and Methods

2.1. Materials

In this study, a 304 stainless-steel rod with a diameter of 5 mm was selected as the experimental material. Prior to laser processing, the samples to be treated must undergo a preliminary preparation stage. The following steps are involved in the processing:

1. The CNC medium wire cutting machine (HA400U, Suzhou Sanguang Technology Co., Ltd., Suzhou, China) was employed to cut samples of stainless-steel body of revolution with a diameter of 5 mm and a length of 360 mm.
2. Subsequently, the samples must be subjected to ultrasonic cleaning in a sequence of solutions, namely an acetone solution, an anhydrous ethanol solution, and deionized water.
3. Subsequently, the sample is placed in a drying oven for a period of 30 min to facilitate complete drying.

The smooth stainless-steel sample with equal diameters obtained after the aforementioned preprocessing can be processed with a laser marking machine for the purpose of creating a secondary fractal drag-reduction structure.

2.2. Secondary Fractal Structure Extraction

One branch of fractal theory is fractal graphics, which concerns itself with the local properties of a system or structure, as well as the similarity between local structures and the overall structural properties. This is the concept of self-similarity, as it applies to fractal structures. Such self-similarity is evident in the natural world, as exemplified by plants and trees. The structure of the branches is analogous to the overall structure of the trunk, and the branching structure of the branches is also analogous to the overall structure of the trunk. This self-similarity can be extended to structures such as tree roots, branches, leaf veins, etc. (see Figure 2a), exemplified by a snowflake derived from the Von Koch self-similarity fractal curve [36]. The secondary fractal structure that forms the basis of this study was inspired by the intricate patterns observed in leaf veins. As a type of fractal structure, the leaf-vein structure is selected for analysis on the basis of its symmetrical lateral veins, as illustrated in Figure 2b. In this study, the primary main groove is identified as the main vein of the leaf vein, while the secondary lateral groove is identified as corresponding to the lateral

vein [37]. As a consequence of the constraints imposed by the processing difficulty, the design of a third-order groove was not feasible. Consequently, the topological model was simplified to a secondary fractal structure. The two-level classification composite-structure model is illustrated in Figure 1. The distance between the main grooves of the first level is designated as S, the width of the main groove is represented by D, and the width of the V-groove on the side of the second level is represented by d. Due to the relatively small size of d, the influence of factors such as scanning times and scanning paths on the drag-reduction performance is not considered separately in laser machining; instead, it is considered together with the main groove of the primary plane. Therefore, λ is set as the width ratio of the first-level main groove to the second-level side groove, i.e., $\lambda = d/\mathrm{D}$. The angle between the first-level main groove and the V-shaped groove on the second-level side groove is α, and the distance between adjacent second-level side grooves is L.

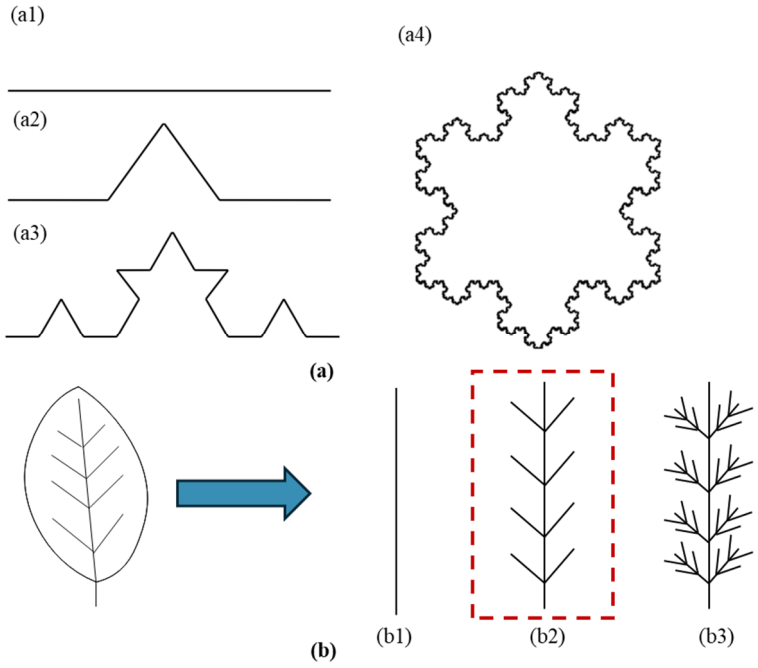


Figure 2. Self-similar fractal structure: (**a1**–**a4**) snowflake fractal structure based on the Von Koch curve; (**b1**–**b3**) self-similar fractal leaf-vein structure.

2.3. Sample Preparation

2.3.1. Fiber Laser Marking Machine

In this study, the YLP-ST20E fibre laser marking machine was selected as the instrument of choice, equipped with a high-precision multi-function worktable prior to installation. The worktable is equipped with multiple screw holes, allowing the installation of a dedicated fixture platform. The formation of V grooves necessitates a specific depth; therefore, power equipment with a maximum power of 20W is selected for processing. The term 'laser scanning speed' is used to describe the distance traversed by the laser beam in a given time period. A comparison of the two-dimensional and three-dimensional morphology images of stainless-steel surfaces processed at varying laser scanning speeds revealed a correlation between scanning speed and the continuity of spot etching on the processed surface. As the scanning speed increased, the continuity of the spot etching decreased, resulting in a gradual transition from a continuous groove structure to a punctual pit structure. Accordingly, a lower scanning speed of 200 mm/s was selected. In this study, a laser pulse frequency of 20 kHz was selected in order to maintain a moderate level of laser pulse frequency, with a wavelength of 1064 nm and a spot size of 50 μm.

2.3.2. Equal Diameter Body of Revolution Positioning Device

In this article, a high-precision punch former is employed as an auxiliary tool for the rotary machining of stainless-steel bodies of revolution of equal diameter. The structure of the apparatus is illustrated in Figure 3. The secondary fractal composite structure on the surface of the stainless-steel body of revolution is achieved through the adjustment of the rotation angle of the high-precision punch former during the machining process. According to the circumference calculation formula, the surface circumference of the stainless-steel body of revolution can be calculated. This is combined with the structural dimensions of the secondary fractal structure and the V-shaped groove structure to determine the single rotation angle during machining. Following a sufficient number of rotations, a complete simulated secondary fractal composite drag-reduction structure can be obtained. It is essential to guarantee the accuracy of coaxiality during the machining of cylindrical workpieces. One end of the workpiece is secured with the aid of a high-precision punch former, with the specimen then fixed in the fixed block of the punch former. The remaining end is positioned with the aid of a tip. In consideration of the unequal height between the tip and the punch former, the requisite dimensions of the auxiliary positioning component must be calculated in accordance with the specific parameters of the high-precision punch former. The sample, which has been previously positioned using auxiliary positioning tools, is then processed using a laser etching method applied to the surface of the stainless-steel body of revolution (as shown in Figure 4). The focusing handle shaft should be rotated in order to adjust the focal length and preview the processing shape. This will ensure that the laser spot corresponds to the axis position on the surface of the stainless-steel body of revolution, and that the spot is bright and not blurred. At this juncture, it is necessary to adjust the angle of the rotary table in order to facilitate the processing of the secondary fractal composite structure on the surface of the stainless-steel body of revolution.

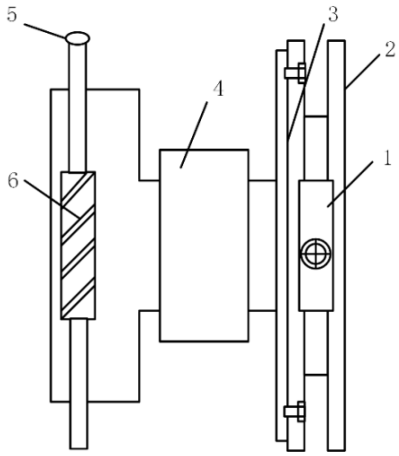


Figure 3. Structure of the punch former: (1) positioning block; (2) rotary table; (3) indexing ring; (4) coupling; (5) rotary handle; (6) worm gear.

2.4. Sample Characterization

The utilisation of the intelligent ultra-depth 3D digital microscope (ZEISS Smart Zoom 5) and laser confocal microscope (CLSM, ZEISS LSM 700) (as illustrated in Figure 4 was recommended for morphology observation and size measurement. An eyepiece with 1000× magnification enables the ultra-depth 3D digital microscope to achieve a resolution of up to 1 μm. The device is capable of continuously capturing multiple images from varying heights, subsequently synthesising the obtained data to generate a three-dimensional representation of the measured object's morphology. The instrument is suitable for measuring the depth, width, and contour curve of V-shaped grooves. The laser confocal microscope is equipped with a 405 nm laser light source, which enables the rapid acquisition of three-dimensional morphology information of the sample surface and the measurement of geometric parameters, including size, angle, and volume. The resolution can reach

0.1 μm to 0.2 μm. The characterisation of the microstructure of the sample surface is conducted using scanning electron microscopy (SEM, Zeiss-EVOMA25, Jena, Germany). The instrument is capable of reaching a maximum acceleration voltage of 20 kV, a maximum amplification factor of 20,000 times, and a maximum resolution of 3 nm. When electrons are incident upon the surface of a material, a number of signals are excited, including Auger electrons (AuE), secondary electrons (SE), backscattered electrons (BSE), and characteristic X-rays. Of these, Auger electron signals can be employed for the analysis of light elements, secondary electrons for the analysis of surface morphology, backscattered electrons for the analysis of material lattice orientation, and characteristic X-rays for the analysis of heavy elements. The Smart EDX SEM energy spectrometer attachment enables the detection of all elements subsequent to carbon, thus facilitating the analysis of the elemental distribution on the surface of the sample. The three-dimensional morphology and size parameters of the sample surface were obtained using a super-depth microscope. The surface roughness was obtained using a confocal laser microscope.



Figure 4. Working area of fibre laser marking machine.

2.5. Drag Measurement

The objective of this study is to examine the drag-reduction capabilities of a secondary fractal composite structure on the surface of stainless-steel bodies of revolution. A device for evaluating drag-reduction performance was designed, and the PIV (Particle Image Velocimetry) method was employed for the assessment of the fluid flow field. The transparent channel was selected for use in the experimental test section of the device, as this facilitates the tracking of particles and the acquisition of images, as illustrated in Figure 5. The test channel is comprised of three primary components: an upper cover plate, a lower bottom plate, and a gasket. The upper cover plate is manufactured from transparent acrylic (PMMA polymethyl methacrylate) and is cylindrical in shape. The lower bottom plate is constructed from aluminium alloy, as are the Y-shaped components on either side of the bottom plate. The gasket material is silicone. In order to utilise the same watershed for experimental testing and numerical simulation, while accounting for the influence of the wall surface on the experimental measurement outcomes, the internal configuration of the test channel has been designed as a hollow cylindrical structure, with a diameter of 16 mm for the hollow watershed. In order to prevent the occurrence of unstable water flow and stress concentration at the inlet, the inlet of the flow field is configured to represent a fully developed flow. In practical drag-reduction testing, it is also essential to consider the stability of the water flow in the vicinity of the inlet and outlet. As the water flows through the pipe and the inlet and outlet in the channel, there are notable alterations in its flow state and channel cross-section. In order to guarantee a sufficient and stable flow in the test section, the inlet and outlet are positioned at each end of the drag-reduction channel, at a distance of 400 mm. Two apertures, with a diameter of 9.5 mm and a G-thread, are located

at the inlet and outlet. The aforementioned components are connected to plastic hoses via metal connectors, thus facilitating the transport of the fluid. Two Y-shaped support brackets are affixed to the base plate for the purpose of providing support and securing the stainless-steel rod throughout the course of the test. The fundamental principle of PIV technology is the introduction of minute tracer particles into the fluid, which must exhibit excellent followability within the fluid. The laser chip light source is capable of illuminating the tracer particles within the watershed, which can then be observed by a high-speed camera in order to obtain a motion image of the tracer particles. By utilising cross-correlation algorithms and image processing techniques, the instantaneous velocity of each point within the watershed can be calculated based on the distance of particle movement between two frames, one preceding and one following the observation. Subsequently, the flow field characteristics are analysed through the utilisation of velocity vector diagrams. Figure 6 provides a schematic representation of the PIV testing device.

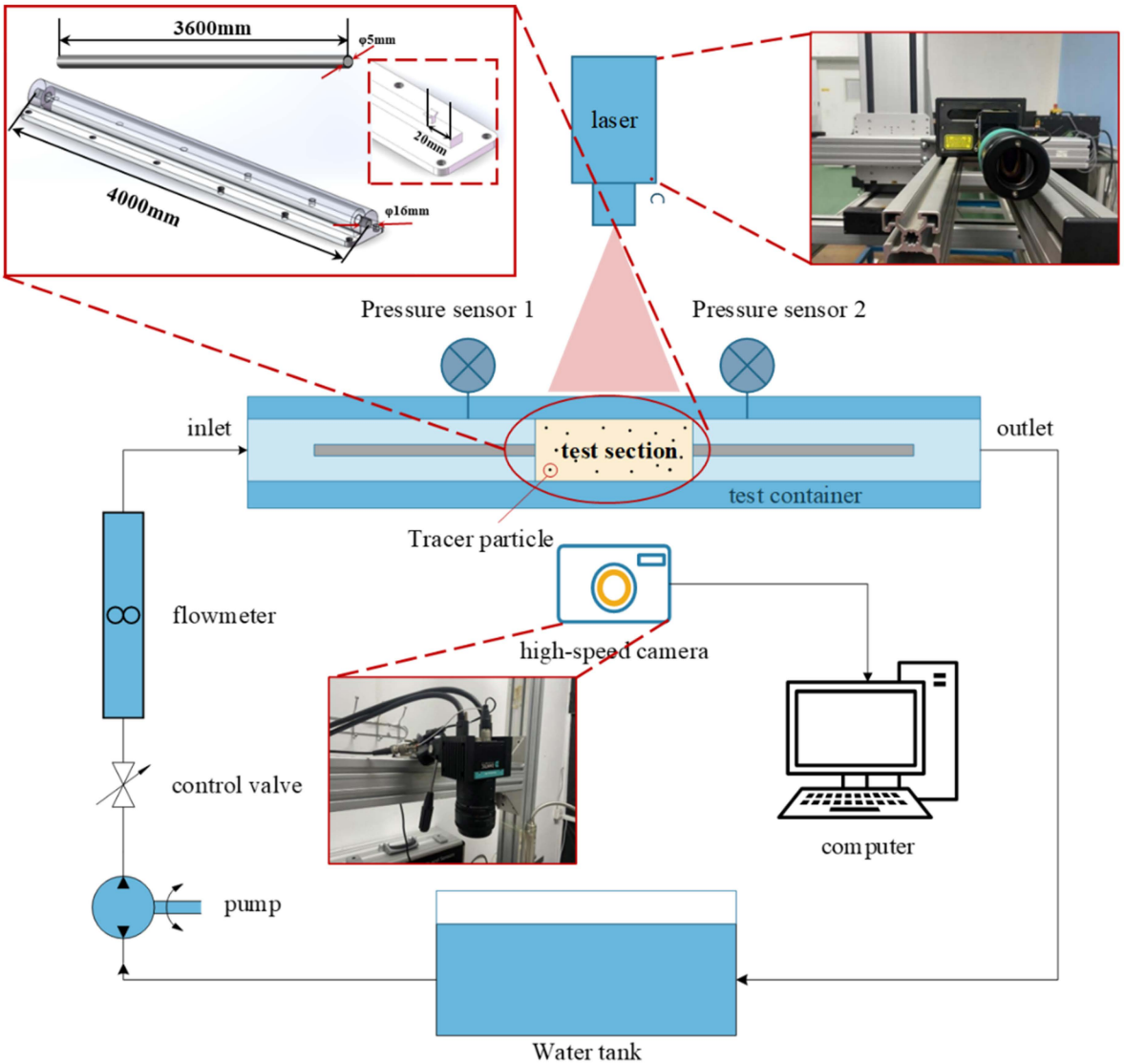


Figure 5. Schematic diagram of drag-reduction performance testing device.

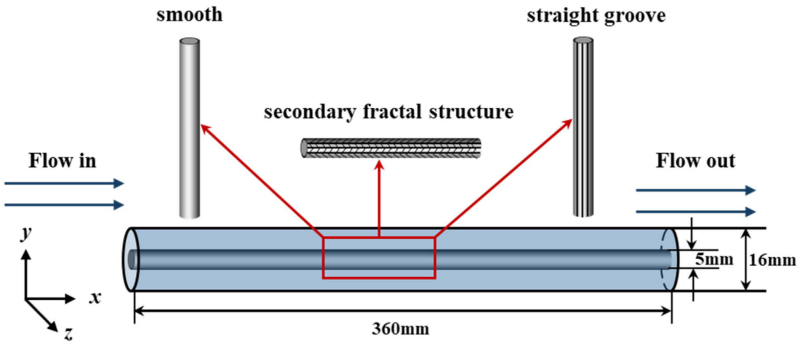


Figure 6. Numerical-simulation fluid-domain setting.

3. Numerical Simulation

3.1. Model Building and Boundary Setting

Numerical simulation employs the identical flume utilized in the experimental test section. This flume features an internal hollow diameter of 16 mm and a stainless-steel rod diameter of 5 mm, collectively forming a circular flow channel, as illustrated in Figure 6. In the simulation calculation process, to circumvent the potential for unstable water flow and stress concentration at the inlet, the inlet of the flow field is set to a fully developed flow, and the wall is designated as a non-slip wall. The velocities in the y and z directions are represented by u, v, and w, respectively. The fluid flows along the *x*-axis at a velocity of u, with a total length of 360 mm. The simulation employs a three-dimensional steady-state approach, with the direction of flow aligned along the *x*-axis. The inlet employs velocity inlet boundary conditions, with disparate operating conditions regulated by varying the Reynolds number. The outlet is configured with pressure outlet boundary conditions, with the pressure set to zero. A pressure-based solver is employed to solve the momentum equation using the SIMPLE algorithm, which utilises a second-order upwind scheme.

3.2. Control Equations and Grid Division

This study employs a variety of analytical techniques, including the use of continuity equations, Reynolds-averaged N-S equations, and realizable k-ε turbulence models, to elucidate the nature of turbulence. The rationale for selecting the Realizable k-ε turbulence model as the turbulence model is that, following a comprehensive comparison and analysis of numerous turbulence models, the Realizable k-ε turbulence model demonstrated the greatest consistency with the actual Reynolds stress and the most accurate simulation of the diffusion velocity of different shapes. It is more closely aligned with the actual circumstances in calculations pertaining to vortices, directional pressure, and separated flows.

The entire computational domain is subdivided into structured meshes. For channels, the grids should be finely divided in order to fully capture the flow field information. For smooth walls, the boundary layer grids should be sufficiently dense to reflect the internal flow conditions of turbulent boundary layers. For watersheds situated at a distance from the wall, the importance of flow field information is relatively low; therefore, the grid can be divided sparsely to reduce computational complexity. A boundary layer should be added to the surface watershed of the secondary fractal composite structure, as illustrated in Figure 7. This should be achieved by setting the thickness of the first layer to 0.05 mm, the grid growth rate to 1.2, and adjusting the number of boundary layers to control the thickness of the boundary layer.

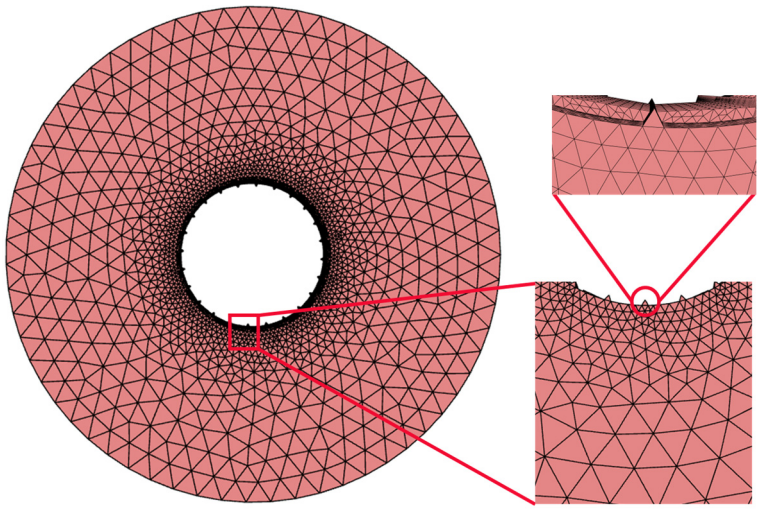


Figure 7. Grid division details.

3.3. Model Reliability Validation

In this study, the realizable k-ε turbulence model was applied to verify the reliability of the selected model. The simulated values of the viscous drag coefficient of the smooth surface on the body of revolution were calculated at different Reynolds numbers, and the obtained data were compared with the theoretical value c calculated by the empirical formula of the viscous drag coefficient of the smooth surface on the body of revolution.

Formula for calculating the empirical viscous resistance value c [38]:

$$c = 0.074\mathrm{Re}^{-\frac{1}{5}}$$

Empirical formula for simulated viscous drag coefficient of smooth wall surface [39]:

$$c_f = \frac{\tau}{0.5\rho u^2}$$

In the formula, c_f is the simulated value of the viscous drag coefficient on a smooth wall surface; τ is the wall shear stress, Pa; ρ is the fluid density, kg/m^3; u is the incident flow velocity, m/s.

The results of the comparison are shown in Table 1. It can be seen from the results that the relative errors are all within ±4%, and the error between the simulated values and the theoretical values is within a reasonable range. Therefore, it is reasonable to use the realisable k-ε model to describe the turbulent wall flow.

Table 1. Comparison of the frictional resistance coefficient on a smooth wall surface.

Re	c	c_f	Absolute Error
4000	0.014087	0.014635	0.038898 (3.9%)
5000	0.013472	0.013624	0.01127 (1.1%)
6000	0.01299	0.012801	−0.01453 (−1.5%)
7000	0.012595	0.012267	−0.02607 (−2.6%)

3.4. Drag-Reduction Analysis

An examination of the leaf veins revealed that the primary structural parameters of different leaves exhibit relatively fixed sizes. Accordingly, when designing a secondary fractal structure, the distance S between the primary main grooves was set to a fixed value (S = 1 mm), the width D of the primary main grooves was selected based on statistical results to have a parameter variation range of 0.1 mm~0.6 mm. The variation range of the angle α between the secondary lateral grooves is 30°~60°, while the variation range

of the distance L between the secondary lateral grooves is 0.6 mm~1.8 mm. Additionally, the primary main grooves and the secondary lateral grooves have a correlation coefficient of λ = 0.5~1.0. In a separate experiment, the parameters were subjected to a single factor analysis in order to narrow down the range of size value selection, as illustrated in Figure 8. Subsequently, orthogonal tests were conducted using the narrowed-down range of parameter size values.

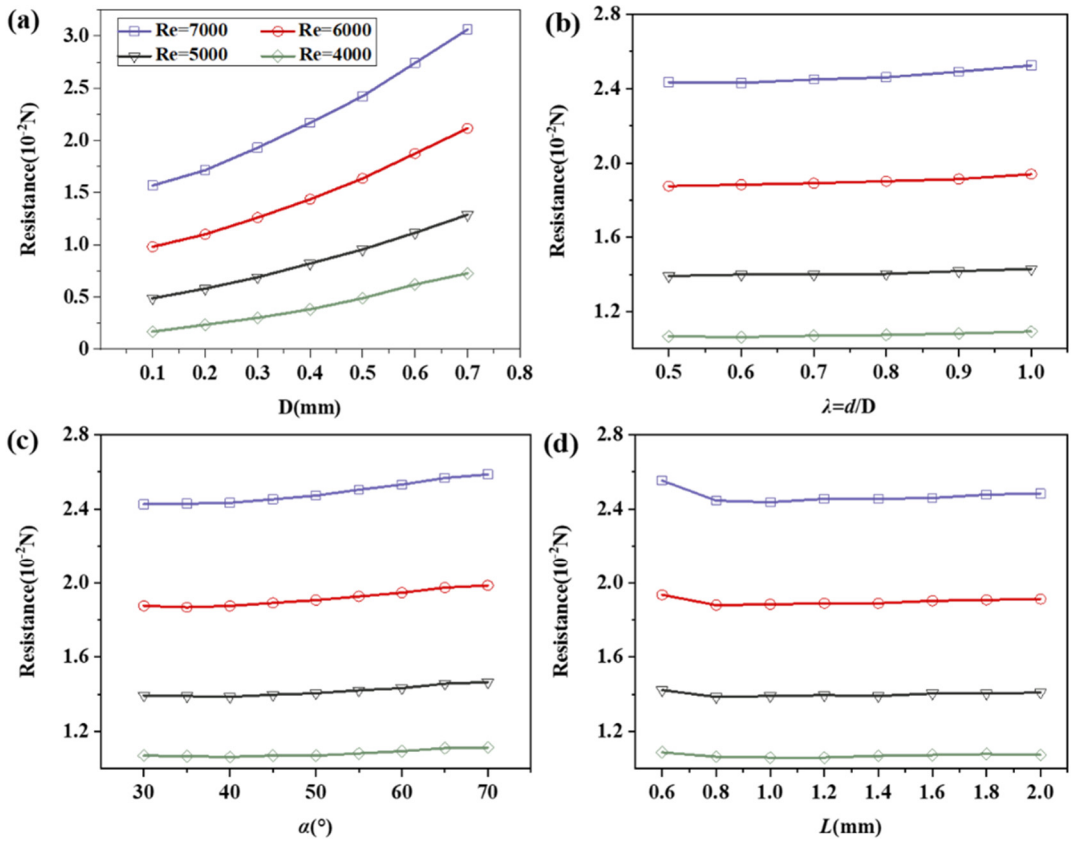


Figure 8. Surface resistance for different parameters of the secondary fractal structure: (**a**) D; (**b**) λ; (**c**) α; (**d**) L.

Figure 8 illustrates that, at a given Reynolds number, the four parameters exert disparate influences on the surface resistance of the secondary fractal composite structure. However, at varying Reynolds numbers, the four parameters exhibit a consistent influence trend on the surface resistance, with a higher Reynolds number indicating an elevated surface resistance. The four parameter levels with the best performance in each experimental factor group should be selected, that is, the level with the smaller surface resistance by the secondary fractal composite structure on the body of revolution surface. An orthogonal experiment should then be designed, with the levels being D = 0.1 mm, 0.2 mm, 0.3 mm, 0.4 mm; λ = 0.5, 0.6, 0.7, 0.8, 0.9, 1. The levels of the four factors were set as follows: D = 0.7, 0.8; α = 30°, 35°, 40°, 45°; L = 0.8, 1.0, 1.2, 1.4. The results of the orthogonal experiments demonstrated that the four factors exerted a varying influence on the surface resistance value of the secondary fractal composite structure of the stainless-steel body of revolution. The order of significance was D > α > L > λ. The width of the primary main groove exerts the most significant influence on the drag-reduction effect of the surface of the secondary fractal composite structure of the stainless-steel body of revolution, with a level of significance of 0.25. The influence of other factors can be disregarded and treated as an error term. Accordingly, on the basis of the significance level of the influence observed in the simulation, D will be selected as the primary structural parameter to be controlled during the machining process. Given that λ = d/D, it follows that when D undergoes a change

in size, d also undergoes a corresponding change. Although the machining parameters change by one unit, during the machining process, it is equivalent to d also changing accordingly. Therefore, according to the results of the orthogonal experiment, when the parameter values are selected as D = 0.1 mm, λ = 0.5, α = 40°, L = 1.0 mm, the resistance value on the surface of the secondary fractal composite structure is the smallest.

As illustrated in Figure 9a, the surface of the equal-diameter body of revolution is characterised by straight grooves, and the trend of resistance distribution is analogous to that observed in the secondary fractal composite structure. For a given Reynolds number, an increase in groove width results in a proportional increase in resistance. Conversely, for a fixed groove width, an increase in Reynolds number leads to an increase in resistance. However, the rate of increase in resistance for straight grooves is less pronounced than that observed for the secondary fractal structure. At a Reynolds number of 7000, the maximum resistance is lower than that observed for the secondary fractal structure.

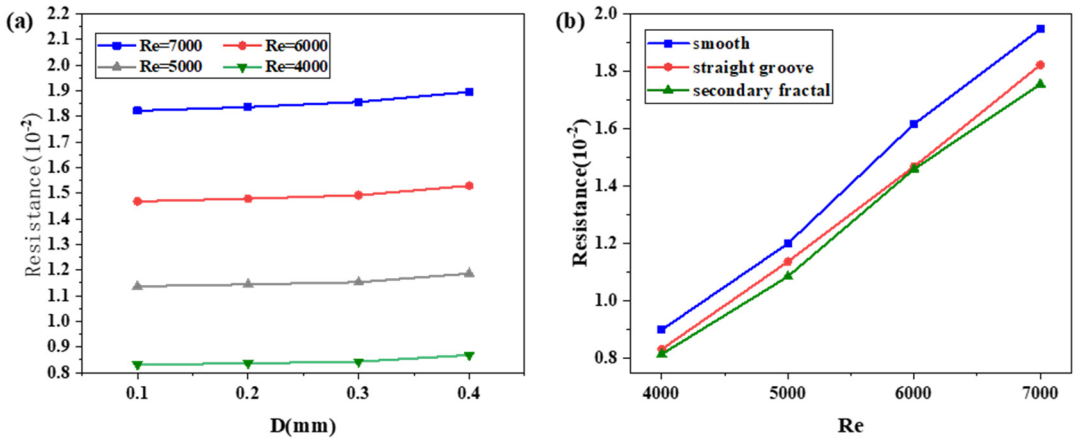


Figure 9. Straight groove resistance situation: (**a**) different-D single-straight-groove resistance; (**b**) surface drag resistance of three structures with different Reynolds numbers.

As illustrated in Figure 9b, the surface resistance of a smooth stainless-steel body of revolution, the surface resistance of stainless-steel bodies of revolution with only straight grooves (primary main grooves) and the optimal surface resistance values of secondary fractal composite structures are obtained at varying Reynolds numbers. It was determined that at a given Reynolds number, the surface resistance of secondary fractal composite structures is the lowest, and the drag-reduction rate is the highest. No clear pattern emerges in the change of the drag-reduction rate of the primary main grooves stainless-steel body of revolution at different Reynolds numbers.

4. Results and Discussion

4.1. Laser Processing Process Parameters

4.1.1. Laser Processing Path

The experiment demonstrated that the optimal laser power for groove formation was 20 W, with a scanning speed of 200 mm/s. Primarily, in order to guarantee the formation of a smooth V-shaped cross-section of the groove, a method of layered scanning and the reduction of scanning lines in different layers was employed. Three processing paths were selected. The initial method entails a reduction in the number of lines on each side of the subsequent layer, with a reduction of one line on each side, relative to the previous layer. This reduction is then applied progressively until the number of lines is reduced to one. The second method entails a reduction in the number of lines on each side by two in comparison to the preceding layer, until the number of lines is reduced to one. The third method involves a reduction in the number of lines in each subsequent layer by four on each side of the first layer, until the number of lines is reduced to one. Secondly, in order to ensure the width of the groove, the scanning path for the first layer of laser processing is

selected and fixed according to the width of the V-shaped groove. The dimensions of the scanning path are as follows: D = 0.1 mm for 5 lines, D = 0.2 mm for 11 lines, D = 0.3 mm for 15 lines, and D = 0.4 mm for 21 lines. The initial scanning path is selected for the primary groove of the first level, the subsequent scanning path is selected for the secondary groove of the second level when D = 0.1 mm, and the subsequent scanning path is selected for D = 0.2, 0.3, 0.4. The resulting depth is illustrated in Table 2.

Table 2. Depth of first-level main groove and second-level lateral groove for different processing paths.

Path Combination	V-Groove Depth (μm)							
	D = 0.1 mm		D = 0.2 mm		D = 0.3 mm		D = 0.4 mm	
	Main	Lateral	Main	Lateral	Main	Lateral	Main	Lateral
1	86.96	70.01	172.34	160.58	242.58	231.40	323.45	297.58
2	84.19	48.74	174.68	140.62	234.23	185.73	312.93	260.64
3	—	—	167.07	92.16	236.64	152.82	318.46	201.62

As illustrated in Figure 10, the surface morphology of V-shaped grooves processed via three distinct scanning paths was observed. It can be observed that when the side length D of the primary main grooves is 0.1 mm, utilising the second scanning path scheme results in the depth of the second-level lateral groove being approximately 0.5 times the depth of the primary main grooves. When D equals 0.2 mm, 0.3 mm, and 0.4 mm, the third scanning path scheme allows for the depth of the secondary lateral groove to be approximately 0.5 times the depth of the primary main groove. From a depth perspective, although the ratio of the depth of the V-shaped groove of the secondary lateral vein to that of the V-shaped groove of the primary main groove is slightly greater than 0.5 with the increase in the width of the primary main groove, it is not completely equal. However, reducing the number of grooves in each layer too much cannot guarantee the smoothness of the V-shaped groove slope. Therefore, the method of reducing more scanning lines was not selected.

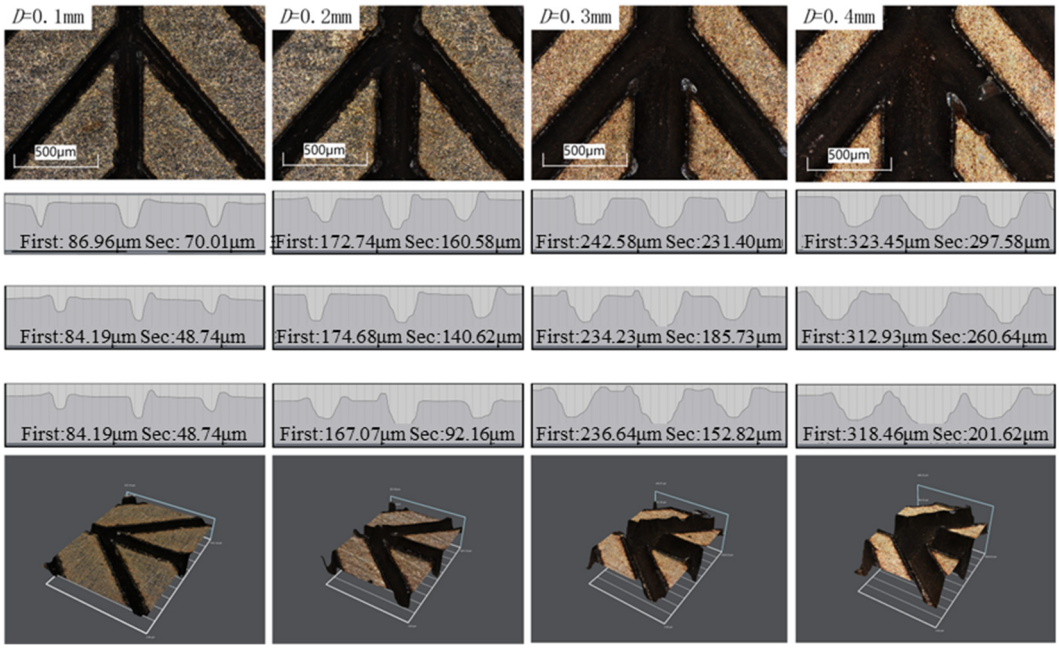


Figure 10. V-shaped groove contour maps corresponding to different scanning paths.

4.1.2. Scanning Times

Once the scanning path was selected, Table 3 illustrates the depth of the secondary fractal grooves on the surface of the stainless-steel equal-diameter body of revolution, processed at different scanning times. It can be observed that when the laser scanning frequency is 10 times, the first stage main pulse edge length D = 0.1 mm and D = 0.2 mm can satisfy the requirement that the ratio of the second stage lateral groove width to the first stage main groove width λ be close to 0.5. Similarly, when the scanning frequency is 15, D = 0.3 mm and D = 0.4 mm can also bring λ closer to 0.5.

Table 3. Optimization of surface parameters for stainless-steel round rod.

Number of Scans	V-Groove Depth (μm)							
	D = 0.1 mm		D = 0.2 mm		D = 0.3 mm		D = 0.4 mm	
	Main	Lateral	Main	Lateral	Main	Lateral	Main	Lateral
20 times	112.50	56.80	216.98	126.29	325.55	214.92	362.85	297.58
15 times	92.95	55.33	202.11	103.70	260.34	192.77	332.93	222.64
10 times	85.00	46.70	172.65	90.75	226.70	156.66	318.46	196.09

4.1.3. Sample Surface Morphology

Figure 11a–c demonstrate the three-dimensional morphology of the secondary fractal structure surface of the stainless-steel body of revolution under a laser confocal microscope at 10, 15, and 20 laser marking times, respectively. The vivid colour contrast facilitates a more intuitive comprehension of the relationship between the processing depth of the stainless-steel rod surface and the number of marking times.

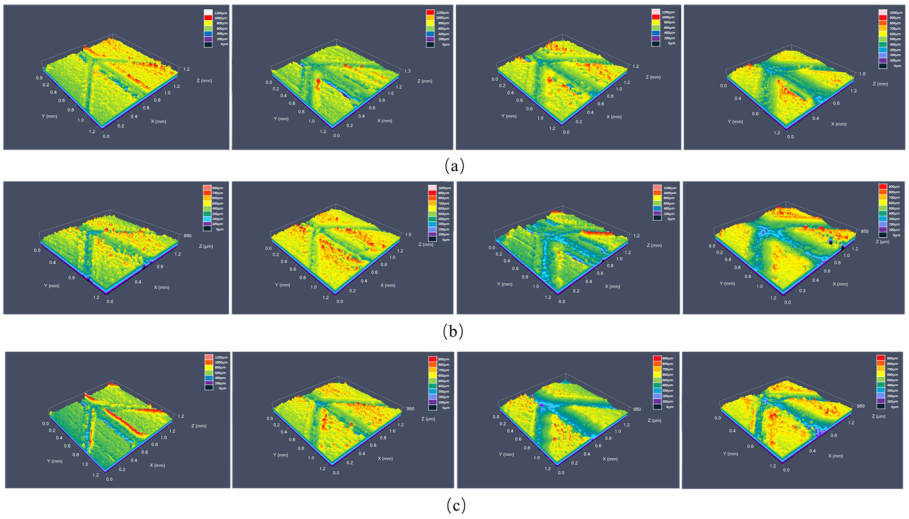


Figure 11. Three-dimensional surface morphology of stainless-steel rotational drag-reduction structure with different scanning times: (**a**) 10 times; (**b**) 15 times; (**c**) 20 times.

In order to investigate the morphology of the V-shaped groove edge and the flatness of the tapered surface of the groove, various regions of the test specimen were characterised and analysed using an electron scanning microscope. As shown in Figure 12a, area 1 represents the overall situation of the primary main vein groove; area 2 represents the inclined surface area of the groove, where the edge of the groove has accumulated molten metal due to laser processing; area 3 is the molten area; area 4 is the unstructured area on both sides of the groove. Figure 12a shows the surface morphology of the V-shaped grooves on the surface of the stainless-steel body of revolution after scanning 10 times, with side lengths of D = 0.1 mm, D = 0.2 mm, D = 0.3 mm, and D = 0.4 mm in area 1–4 under scanning electron microscopy at different magnifications. It can be seen that the amount

and size of the surface melt at D = 0.1 mm, D = 0.2 mm, D = 0.3 mm, and D = 0.4 mm are not significantly different from the total size. The amount of surface melt increases with the size of the V-shaped groove. The continuity of the groove slope surface is relatively good, and a small number of traces of the scanning path can be seen. Figure 12b shows the surface morphology of area 1–4 at different magnifications under a scanning electron microscope for the V-shaped grooves on the surface of a stainless-steel body of revolution with laser scanning times of 15, side lengths of D = 0.1 mm, D = 0.2 mm, D = 0.3 mm, and D = 0.4 mm, respectively. It can be seen that the distribution of the surface melt is basically similar for D = 0.1 mm, D = 0.2 mm, D = 0.3 mm, and D = 0.4 mm, but the distribution pattern of the melt spatter on both sides of the groove is different. At D = 0.1 mm, there is almost no melt splatter on the surface. As the size of the V-groove increases, the amount of molten spatter increases significantly. The V-groove has good continuity in its inclined surface morphology, and the overall surface is smooth and flat. Figure 12c shows the surface morphology of area 1–4 under scanning electron microscopy at different magnifications for V-shaped grooves with side lengths of D = 0.1 mm, D = 0.2 mm, D = 0.3 mm, and D = 0.4 mm on the surface of a stainless-steel body of revolution after 20 laser scans. It can be seen that, at the same scanning frequency, the surface molten material with D = 0.1 mm, D = 0.2 mm, D = 0.3 mm, and D = 0.4 mm increases with the increase in the size of the V-shaped groove (the larger the size, the more repeated the scanning path). The number and size of melt splashes on the unstructured surfaces on both sides also increase with the size of the V-groove, but the overall difference is not significant. The internal slope morphology of the V-groove has good continuity, and there are no defects.

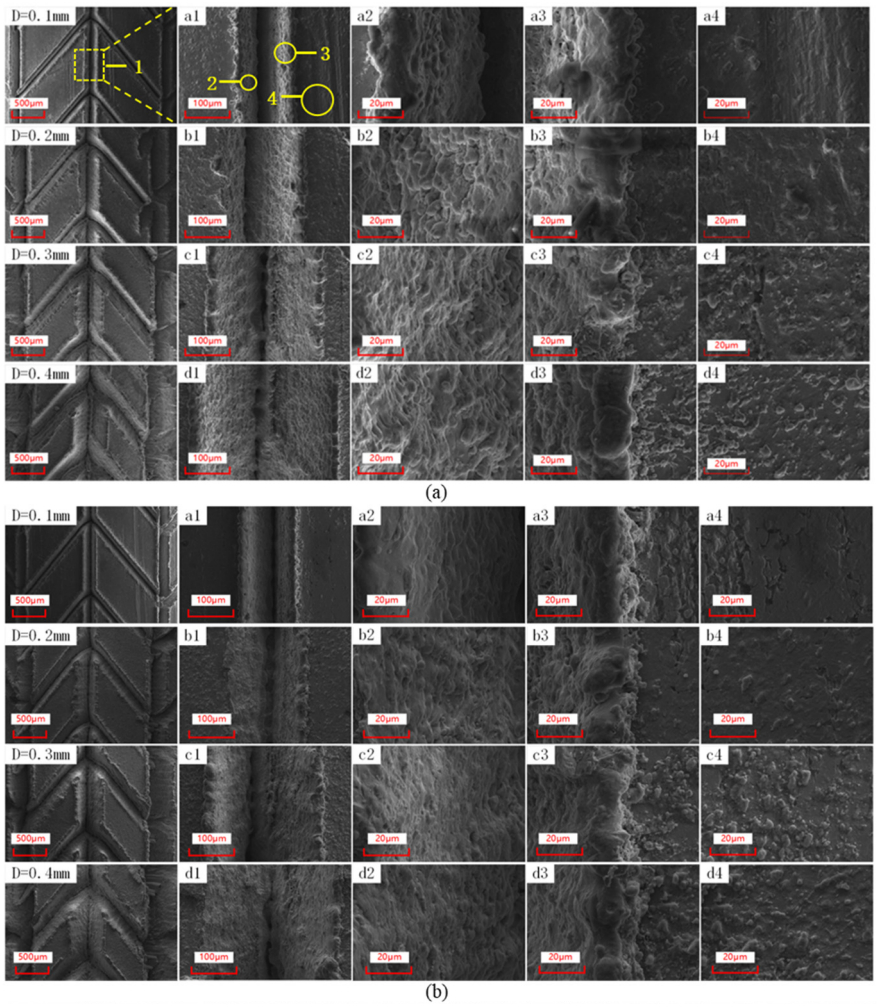


Figure 12. *Cont.*

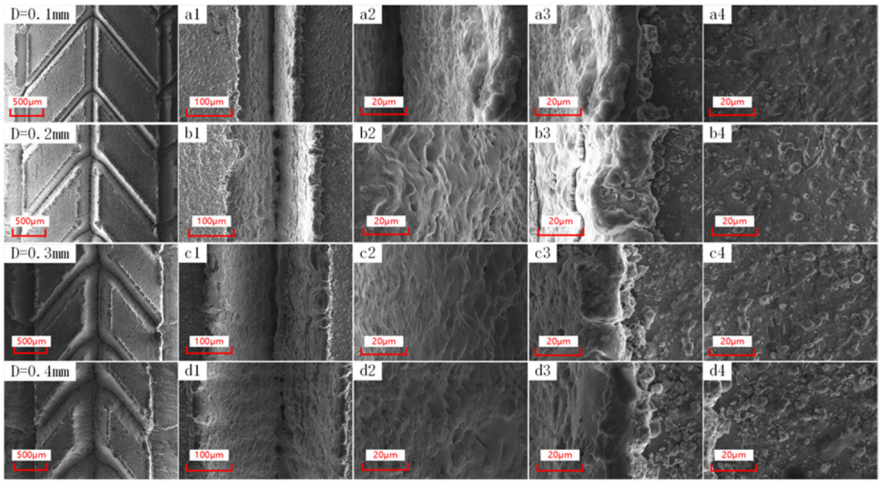


Figure 12. Surface morphology of stainless-steel equal-diameter body of revolution with different laser scanning times: (**a**) 10 times; (**b**) 15 times; (**c**) 20 times.

4.2. Flow Field Test Results and Drag-Reduction Rate Calculation

After PIV testing, the average velocity within a local watershed can be obtained. Combined with the formula, the Reynolds number of the local watershed in the actual test can be calculated. Furthermore, based on the relationship between the coefficient of drag along the path and the Muddy diagram, the formula for calculating the coefficient of drag (λ_D) along the path can be obtained. Due to the use of a straight hollow cylindrical watershed as the test environment in this experiment, it can be assumed that there is no local resistance. The total drag coefficient is the sum of the along path drag coefficient and the local drag coefficient. Therefore, the along path drag coefficient calculated based on the actual test can be used as the total drag coefficient. That is, the ratio of the difference between the surface resistance coefficient λ_{smooth} of the smooth stainless-steel rotary body and the surface resistance coefficient $\lambda_{secondary\ fractal\ structure}$ of the stainless-steel rotary body of the secondary fractal drag-reduction structure to the surface resistance coefficient of the smooth stainless-steel rotary body is used as the drag-reduction rate of the blade-like stainless-steel bar. The drag-reduction rate of the surface of the secondary fractal drag reducing stainless-steel body of revolution relative to the surface of the ordinary smooth stainless-steel body of revolution can be defined as η [40,41]:

$$\mathrm{Re} = \frac{\rho v D}{\mu}$$

$$\lambda_D = \frac{0.3164}{\mathrm{Re}^{0.25}}$$

$$\eta = \frac{\lambda_{smooth} - \lambda_{secondary\ fractal\ structure}}{\lambda_{smooth}} \times 100\%$$

The photographs taken by the CCD camera were analysed for particle velocity detection using PIV Lab software (Matlab R2019a), and the average velocity of the test area was determined. Based on the average velocity of the watershed, the Reynolds number, turbulent drag coefficient and drag-reduction rate of stainless-steel bodies of revolution with secondary fractal structures compared to smooth stainless-steel bodies of revolution were calculated. Table 4 shows the test data and calculation results of the smooth stainless-steel body of revolution surface, while Tables 5–8 show the test data and calculation results of the secondary fractal structure surface with D = 0.1 mm, D = 0.2 mm, D = 0.3 mm, and D = 0.4 mm, respectively.

Table 4. Test data for smooth stainless-steel body of revolution.

Test Number	Average Velocity			
	Re = 4000	**Re = 5000**	**Re = 6000**	**Re = 7000**
1	0.36097	0.44993	0.52828	0.59515
2	0.42122	0.57540	0.63086	0.61399
3	0.41160	0.57352	0.70773	0.71914
4	0.43795	0.51098	0.52927	0.81751
5	0.44161	0.45120	0.47154	0.48551
6	0.36732	0.57527	0.64486	0.60253
7	0.36069	0.47943	0.49476	0.70128
8	0.43819	0.50397	0.44290	0.63612
9	0.44556	0.56381	0.61991	0.52852
10	0.43253	0.46171	0.60865	0.74568
Average speed	0.412	0.512	0.568	0.645
Reynolds number (Re)	4100	5096	5653	6419
resistance coefficient	0.03954	0.03745	0.03649	0.03535

Table 5. Test data for D = 0.1 mm secondary fractal stainless-steel body of revolution.

Test Number	Average Velocity			
	Re = 4000	**Re = 5000**	**Re = 6000**	**Re = 7000**
1	0.45733	0.72189	0.69931	0.81048
2	0.57730	0.51941	0.76588	0.80662
3	0.55030	0.59228	0.64034	0.68363
4	0.44598	0.65465	0.75235	0.80961
5	0.52645	0.55030	0.72023	0.80533
6	0.49994	0.57027	0.70876	0.78566
7	0.45478	0.73159	0.82073	0.84169
8	0.48976	0.63038	0.67166	0.81230
9	0.52333	0.59965	0.62894	0.81550
10	0.50930	0.68509	0.68273	0.74079
Average speed	0.503	0.626	0.709	0.792
Reynolds number (Re)	5006	6230	7056	7882
resistance coefficient	0.03762	0.03561	0.03452	0.03344
Resistance interpolation	0.00192	0.00184	0.00197	0.00191
Drag reduction rate	4.86%	5.15%	5.28%	5.40%

Table 6. Test data for D = 0.2 mm secondary fractal stainless-steel body of revolution.

Test Number	Average Velocity			
	Re = 4000	**Re = 5000**	**Re = 6000**	**Re = 7000**
1	0.44102	0.46867	0.56233	0.67406
2	0.49516	0.53323	0.55002	0.8164
3	0.35308	0.44709	0.54035	0.67842
4	0.36609	0.49445	0.55529	0.7384
5	0.31199	0.39602	0.52205	0.74131
6	0.38228	0.49046	0.56314	0.73916
7	0.3563	0.5144	0.52525	0.56896
8	0.52337	0.45386	0.5338	0.64904
9	0.33071	0.43252	0.52431	0.62189
10	0.26748	0.41403	0.53812	0.58946
Average speed	0.383	0.464	0.541	0.682
Reynolds number (Re)	3812	4618	5384	6768
resistance coefficient	0.04026	0.03838	0.03694	0.03488
Resistance interpolation	−0.00072	−0.00093	−0.00045	0.00047
Drag reduction rate	−1.82%	−2.48%	−1.23%	1.33%

Table 7. Test data for D = 0.3 mm secondary fractal stainless-steel body of revolution.

Test Number	Average Velocity			
	Re = 4000	**Re = 5000**	**Re = 6000**	**Re = 7000**
1	0.32756	0.34119	0.42285	0.64374
2	0.38912	0.44748	0.48111	0.70484
3	0.3773	0.53695	0.52762	0.74419
4	0.35938	0.4242	0.56952	0.53798
5	0.37468	0.36984	0.52729	0.60952
6	0.38113	0.45139	0.57502	0.63266
7	0.34326	0.46054	0.55806	0.68471
8	0.32951	0.49841	0.6245	0.55643
9	0.33812	0.46586	0.49621	0.60439
10	0.30167	0.41964	0.53458	0.6155
Average speed	0.352	0.442	0.531	0.633
Reynolds number (Re)	3503	4399	5285	6300
Resistance coefficient	0.04113	0.03885	0.03711	0.03551
Resistance interpolation	−0.00159	−0.0014	−0.00062	−0.00016
Drag reduction rate	−4.02%	−3.74%	−1.70%	−0.45%

Table 8. Test data for D = 0.4 mm secondary fractal stainless-steel body of revolution.

Test Number	Average Velocity			
	Re = 4000	**Re = 5000**	**Re = 6000**	**Re = 7000**
1	0.33069	0.4923	0.43195	0.52986
2	0.33839	0.33079	0.51506	0.60203
3	0.3043	0.35411	0.57481	0.6523
4	0.35246	0.48291	0.59166	0.70432
5	0.29289	0.36731	0.57685	0.65528
6	0.2872	0.36715	0.56839	0.6342
7	0.29028	0.32244	0.59509	0.60786
8	0.26426	0.33789	0.45728	0.5772
9	0.38681	0.50584	0.47608	0.58614
10	0.30283	0.35699	0.43223	0.53643
Average speed	0.315	0.392	0.522	0.609
Reynolds number (Re)	3135	3901	5195	6061
Resistance coefficient	0.04228	0.04004	0.03727	0.03586
Resistance interpolation	−0.00274	−0.00259	−0.00078	−0.00051
Drag reduction rate	−6.93%	−6.92%	−2.14%	−1.44%

By comparing the drag-reduction rates in Tables 5–8, it can be seen that only the secondary fractal structure with D = 0.1 mm has a drag-reduction effect on the surface of the stainless-steel body of revolution, while the secondary fractal structures with D = 0.2 mm, D = 0.3 mm, and D = 0.4 mm not only have no drag-reducing effect but also have a certain drag increasing effect; as the size of the first-level main groove width D increases, the surface drag reducing effect becomes weaker and the drag increasing effect becomes stronger; at different Reynolds numbers, the surface drag coefficient and drag reducing effect are different. As the Reynolds number increases, the drag-reduction rate of the surface of the stainless-steel body of revolution with a secondary fractal structure of D = 0.1 mm also increases. At D = 0.2 mm, D = 0.3 mm, and D = 0.4 mm, although these sizes of secondary fractal structures only have the effect of increasing drag, their drag-reduction effect also decreases with increasing Reynolds number.

4.3. PIV Testing of Velocity Field on the Surface of Equal Diameter Stainless-Steel Body of Revolution

Figure 13 shows the velocity vector diagram of the secondary fractal structure stainless-steel body of revolution at different Reynolds numbers when D = 0.1 mm. It can be clearly

seen that at Re = 4000 there are small vortices and turbulent spots in the watershed. As the Reynolds number increases, the number of small eddies in the watershed increases, and the velocity vector cloud map shows that the velocities of the eddies and turbulent spots increase accordingly. By observing the turbulent boundary layer on the surface of the simulated leaf-vein structure at different Reynolds numbers, it was found that Re was in the range of 4000~7000. The experimentally obtained turbulent boundary layer was basically consistent with the theoretical turbulent boundary layer. Near the surface of the secondary fractal structure, there was a laminar bottom layer, and the watershed was filled with small eddies and turbulent spots.

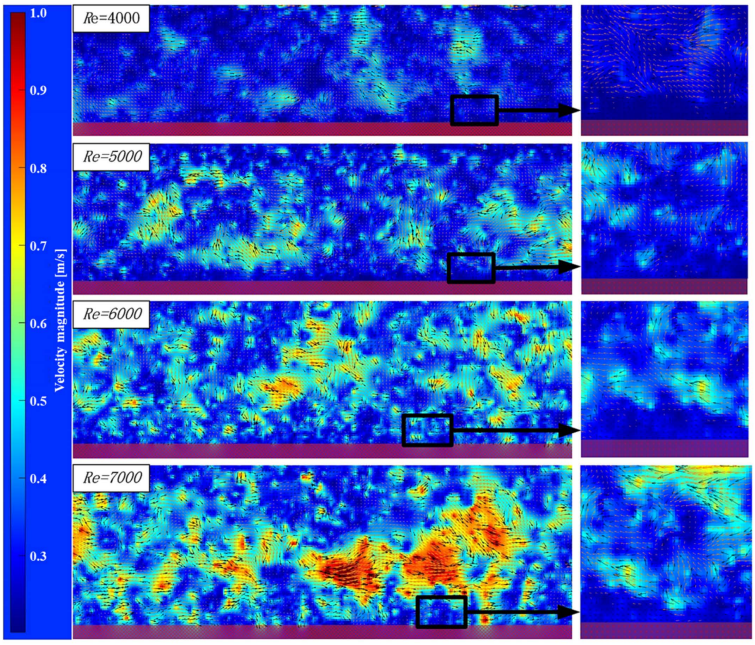


Figure 13. Surface velocity vector diagram of stainless-steel body of revolution with secondary fractal structure at different Reynolds numbers.

Figure 14 shows the velocity vector diagrams of the secondary fractal stainless-steel body of revolution at D = 0.1 mm, D = 0.2 mm, D = 0.3 mm, and D = 0.4 mm for the same Reynolds number. It can be seen that vortices and turbulence patches are present in all four sets of velocity vector diagrams in the watershed but show differences at the turbulent boundary layer. When the width of the first-level main channel is D = 0.1 mm, the turbulent boundary layer corresponds to the theoretical turbulent boundary layer consisting of a laminar bottom layer, small vortices and turbulent spots. However, at D = 0.2 mm there is a small amount of disturbance in the laminar boundary layer. As the width of the first-level main groove D increases, the disturbance gradually increases until D = 0.4 mm, when the disturbance in the laminar bottom layer becomes small eddies. The disturbance in the lower layer of the laminar flow increases with the increase in the first main groove edge length, D. The experimental results are in good agreement with the numerical simulation results. This increase in disturbance causes an increase in wall shear force and flow resistance. In addition, from the experimental results, it can be seen that only when D = 0.1 mm, the laminar bottom layer shows stable performance with almost no disturbance phenomenon.

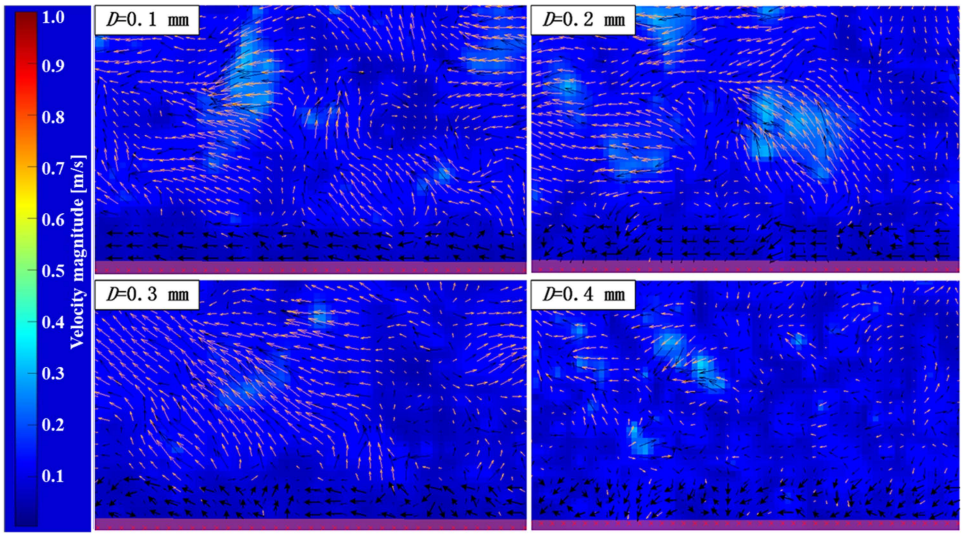


Figure 14. Velocity vector diagram of equal diameter stainless-steel body of revolution with different secondary fractal structures.

4.4. Analysis of Drag-Reduction Mechanism

A synthesis of the findings of numerous scholars reveals two common mechanisms for analysing the drag reduction of grooves. The initial theory is that of the secondary vortex. Lee et al. [42] posit that the majority of streamline vortices are situated above the micro ridge and interact with the extremity of the micro ridge. The rib tip impedes the meridional motion of the flow field vortex, thereby inducing secondary vortices. In comparison with smooth flat plates, the normalized root mean square velocity fluctuations and turbulence energy in the vicinity of the rib tip surface are diminished, resulting in a drag-reduction effect. The second method is the "bulge height theory", which analyses the velocity distribution of the boundary layer of the groove wall from the perspective of velocity gradient, thereby demonstrating the drag-reduction effect of the groove [43].

Comparing the velocity vector diagrams of the smooth stainless-steel body of revolution and the processed stainless-steel body of revolution with a secondary fractal structure. As shown in Figure 15, the laminar bottom layer was enlarged and marked. It was found that the laminar bottom layer on the surface of the stainless-steel body of revolution with a secondary fractal structure tended to be stable, and there were a few small vortices present in the laminar bottom layer on the surface of the smooth stainless-steel body of revolution. Compared with the laminar bottom layer on the surface of the stainless-steel body of revolution with a secondary fractal structure, the latter has better stability in the laminar bottom layer, and the velocity in the laminar bottom layer is slightly higher than that on the smooth surface; that is, the primary main groove causes high-speed bands to appear near the wall of the stainless-steel body of revolution. There are a small number of vortices in the laminar bottom layer on the surface of the smooth stainless-steel body of revolution, which causes the wall shear force to be greater than that of the secondary fractal structure surface, and the surface resistance is greater than that of the secondary fractal structure, thus reflecting the drag-reduction function of the secondary fractal structure.

In comparison to smooth surface bodies of revolution, the secondary fractal composite drag-reduction structure displays high-speed bands with laminar flow properties in the vicinity of the primary main grooves and secondary grooves, resulting in a slight increase in near-wall flow velocity on the surface of the secondary fractal structure relative to smooth surfaces. In the primary main and secondary V-shaped grooves, it was observed that the velocity of the low-speed flow area was nearly zero. In the V-shaped groove with a secondary fractal composite structure and D = 0.1 mm, the low-velocity flow area was observed to occupy the entirety of the V-shaped groove, thereby altering the contact form between the surface of the stainless-steel body of revolution and the liquid, changing from

solid–liquid to liquid–liquid. This resulted in a reduction in frictional resistance, thereby achieving the drag-reduction effect.

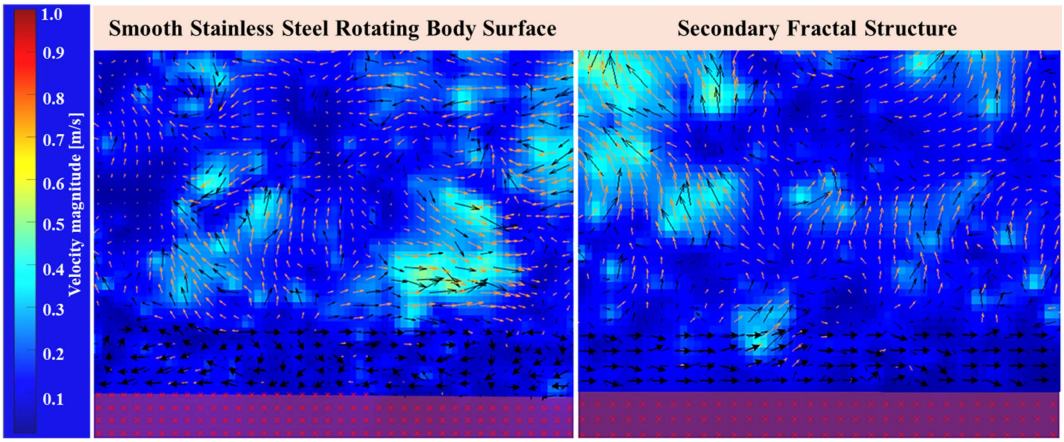


Figure 15. Velocity vector diagram of the surface of a smooth stainless-steel body of revolution and the surface of stainless-steel body of revolution with a secondary fractal structure.

5. Conclusions

In summary, this study combines the secondary fractal topology designed based on the leaf-vein structure with V-shaped grooves to form a secondary fractal composite drag-reduction structure. The structure is processed on the surface of an equal-diameter body of revolution using laser etching and a fixing device. The secondary fractal composite structure was characterised using SEM, a super-depth-of-field microscope, and a laser confocal microscope. The results show that laser processing can process V-shaped grooves with smooth surfaces, but there is splashing of molten material in the unprocessed area. Finally, the drag-reduction performance of the secondary fractal composite structure on the surface of the stainless-steel equal-diameter body of revolution was tested by combining the PIV tracer particle velocimetry drag-reduction testing system. When D = 0.1 mm, it has drag-reduction ability at different Reynolds numbers. The drag-reduction rates at Re = 4000, Re = 5000, Re = 6000, and Re = 7000 are 4.86%, 5.15%, 5.28%, and 5.40%, respectively. Although the drag-reduction rate test results are lower than the numerical simulation results, the distribution of flow velocity in the two flow fields is basically the same. Based on this, the analysis of the drag-reduction mechanism can be carried out.

Author Contributions: Conceptualization, Z.H., Q.Z. and Z.Y.; Methodology, Z.H., Q.Z., X.Z. and Y.W. (Yonghua Wang); Software, Y.W. (Yan Wang), Z.H. and Z.Y.; Validation, Y.W. (Yan Wang), Z.Y. and X.Z.; Formal analysis, Y.W. (Yonghua Wang); Investigation, Z.H. and Q.Z.; Resources, Y.W. (Yan Wang) and Y.W. (Yonghua Wang); Data curation, Z.H.; Writing—original draft, Y.W. (Yan Wang); Writing—review & editing, Y.W. (Yan Wang); Supervision, Y.W. (Yonghua Wang); Funding acquisition, Y.W. (Yonghua Wang). All authors have read and agreed to the published version of the manuscript.

Funding: The projects supported by the Jilin Province Science and the Technology Department (Grant No. 20240302055GX), the National Natural Science Foundation of China (Grant No. 52175264), the Jilin Province Science and Technology Department (Grant No. 20220201054GX and YDZJ202301ZYTS490), the National Natural Foundation of Chongqing province (Grant No. CSTB2022NSCQMSX0506 and CSTB2022NSCQ-MSX1643) for providing financial support for this article.

Institutional Review Board Statement: Not applicable.

Informed Consent Statement: Not applicable.

Data Availability Statement: The data that support the findings of this study are available from the corresponding author upon reasonable request.

Conflicts of Interest: The authors declare no conflicts of interest.

References

1. Hu, S.C.; Shiue, A.; Chuang, H.C.; Xu, T. Life cycle assessment of high-technology buildings: Energy consμmption and associated environmental impacts of wafer fabrication plants. *Energy Build.* **2013**, *56*, 126–133. [CrossRef]
2. Wang, J. *Reviews and Prospects in Turbulent Drag Reduction Over Riblets Surface*; NASA: Washington, DC, USA, 1998; pp. 31–34.
3. Bacher, E.V.; Smith, C.R. *A Combined Visualization-Anemometry Study of the Turbulent Drag Reducing Mechanisms of Triangular Micro-Groove Surface Modifications*; AIAA Paper: Reston, VA, USA, 1985.
4. Walsh, M.J. Viscous Drag Reduction in Boundary Layers. *Prog. Astronaut. Aeronaut.* **1990**, *123*, 203–261.
5. Bechert, D.W.; Hoppe, G.; Reif, W.E. On the drag reduction of the shark skin. In Proceedings of the American Institute of Aeronautics and Astronautics Shear Flow Control Conference, Boulder, CO, USA, 12–14 March 1985; AIAA Press: Reston, VA, USA, 1985.
6. Walsh, M.J. Effect of detailed surface geometry on riblet drag reduction performance. *J. Aircr.* **1990**, *27*, 572–573. [CrossRef]
7. Neumann, D.; Dinkelacker, A. Drag measurements on V-grooved surfaces on a body of revolution in axial flow. *Appl. Sci. Res.* **1991**, *48*, 105–114. [CrossRef]
8. Jung, Y.C.; Bhushan, B. Biomimetic structures for fluid drag reduction in laminar and turbulent flows. *J. Phys. Condens. Matter Inst. Phys. J.* **2010**, *22*, 035104. [CrossRef]
9. Bixler, G.D.; Bhushan, B. Shark skin inspired low-drag microstructured surfaces in closed channel flow. *J. Colloid Interface Sci.* **2013**, *393*, 384–396. [CrossRef]
10. Moalem-Maron, D.; Semiat, R.; Sideman, S. Enhanced heat transfer in horizontal evaporator- condensers with straight-edged grooved tubes. *Desalination* **1980**, *34*, 289–309. [CrossRef]
11. Nishimoto, S.; Bhushan, B. Bioinspired self-cleaning surfaces with superhydrophobicity, superoleophobicity, and superhydrophilicity. *RSC Adv.* **2012**, *3*, 671–690. [CrossRef]
12. Liu, K.; Jiang, L. Bio-Inspired Self-Cleaning Surfaces. *Annu. Rev. Mater. Res.* **2012**, *42*, 231–263. [CrossRef]
13. Lake, J.; King, P.; Rivir, R. Low Reynolds number loss reduction on turbine blades with dimples and V-Grooves. In Proceedings of the 38th Aerospace Sciences Meeting and Exhibit, American Institute of Aeronautics and Astronautics, Washington, DC, USA, 10–13 January 2000.
14. Nitschke, P. *Experimental Investigation of the Turbulent Flow in Smooth and Longitudinal Grooved Pipes*; Fuer Stroemungsforschung; Thesis Max-Planck Institute: Göttingen, Germany, 1983.
15. Rapp, H.; Zoric, I.; Kasemo, B. Microstructured surfaces for drag reduction purposes: Experiments and simulation on rectangular 2D riblets. *Mater. Res. Soc.* **2005**, *899*, 808. [CrossRef]
16. Auteri, F.; Baron, A.; Belan, M.; Campanardi, G.; Quadrio, M. Experimental assessment of drag reduction by traveling waves in a turbulent pipe flow. *Phys. Fluids* **2010**, *22*, 115103. [CrossRef]
17. Tang, F.; Yan, Z.L.; Wang, X.H. Experimental Research on Lift up and Drag Reduction Effect of Streamwise Travelling Wave Wall. *Key Eng. Mater.* **2011**, *483*, 721–726. [CrossRef]
18. Peet, Y.; Sagaut, P.; Charron, Y. Turbulent Drag Reduction using Sinusoidal Riblets with Triangular Cross-section. In Proceedings of the 38th AIAA Fluid Dynamics Conference and Exhibit, Washington, DC, USA, 23–26 June 2008; p. 3745.
19. Dengke, C.; Xianxian, C.; Huawei, C. Controllable deformation based self-adaptive drag reduction for complex surface. *Biosurface Biotribology* **2023**, *9*, 17–23.
20. Chen, D.; Liu, X.; Cui, X.; Zhang, L.; Chen, H. Research progress and development trend of the drag reduction inspired by fish skin. *Prog. Org. Coatings* **2023**, *182*, 107613. [CrossRef]
21. Huang, P.; Dong, G.; Zhong, X.; Pan, M. Numerical investigation of the fluid flow and heat transfer characteristics of tree-shaped microchannel heat sink with variable cross-section. *Chem. Eng. Process. Process. Intensif.* **2020**, *147*, 107769. [CrossRef]
22. Ji, X.; Yang, X.; Zhang, Y.; Zhang, Y.; Wei, J. Experimental study of ultralow flow resistance fractal microchannel heat sinks for electronics cooling. *Int. J. Therm. Sci.* **2022**, *179*, 107723. [CrossRef]
23. Falconer, K.J. *Techniques in Fractal Geometry*; John Wiley: Chichester, UK, 1997.
24. Schumacher, J.F.; Aldred, N.; Callow, M.E.; Finlay, J.A.; Callow, J.A.; Clare, A.S.; Brennan, A.B. Species-specific engineered antifouling topographies: Correlations between the settlement of algal zoospores and barnacle cyprids. *Biofouling* **2007**, *23*, 307–317. [CrossRef]
25. Henoch, C.; Krupenkin, T.; Kolodner, P.; Taylor, J.; Hodes, M.; Lyons, A.; Peguero, C.; Breuer, K. Turbulent drag reduction using superhydrophobic surfaces. In Proceedings of the 3rd AIAA Flow Control Conference, San Francisco, CA, USA, 5–8 June 2006; American Institute of Aeronautics and Astronautics: Washington, DC, USA, 2006.
26. Cui, X.; Chen, D.; Chen, H. Multistage Gradient Bioinspired Riblets for Synergistic Drag Reduction and Efficient Antifouling. *ACS Omega* **2023**, *8*, 8569–8581. [CrossRef]
27. Wang, X.C.; Wan, Y.C. Picosecond laser fabrication of the riblet-array surface texture on Ti64 alloy substrate. *J. Laser Micro Nanoeng.* **2020**, *14*, 206–213.
28. Kietzig, A.M.; Lehr, J.; Matus, L.; Liang, F. *Laser-Induced Patterns on Metals and Polymers for Biomimetic Surface Engineering*; International Society for Optics and Photonics: Bellingham, WA, USA, 2014.
29. Xiao, G.; He, Y.; Huang, Y.; Li, Q. Shark-Skin-Inspired Micro-Riblets Forming Mechanism of TC17 Titanium Alloy with Belt Grinding. *IEEE Access* **2019**, *7*, 107635–107647. [CrossRef]

30. Chen, H.; Zhang, X.; Ma, L.; Che, D.; Zhang, D.; Sudarshan, T. Investigation on largearea fabrication of vivid shark skin with superior surface functions. *Appl. Surf. Sci.* **2014**, *316*, 124–131. [CrossRef]
31. Denkena, B.; Köhler, J.; Wang, B. Manufacturing of functional riblet structures by profile grinding. *CIRP J. Manuf. Sci. Technol.* **2010**, *3*, 14–26. [CrossRef]
32. Zhao, D.Y.; Huang, Z.P.; Wang, M.J.; Wang, T.; Jin, Y. Vacuum Casting Replication of Micro-riblets on Shark Skin for Drag-reducing Applications. *J. Mater. Proc. Technol.* **2012**, *212*, 198–202. [CrossRef]
33. Qin, L.; Hafezi, M.; Yang, H.; Dong, G.; Zhang, Y. Constructing a Dual-Function Surface by Microcasting and Nanospraying for Efficient Drag Reduction and Potential Antifouling Capabilities. *Micromachines* **2019**, *10*, 490. [CrossRef]
34. Soltani-Kordshuli, F.; Miller, C.; Harris, N.; Zou, M. Laser surface texturing of both thin polytetrafluoroethylene coatings and stainless steel substrates for improving tribological properties. *Polym. Test.* **2023**, *117*, 107852. [CrossRef]
35. Sorrentino, L.; Parodo, G.; Turchetta, S. Influence of Laser Treatment on End Notched Flexure Bonded Joints in Carbon Fiber Reinforced Polymer: Experimental and Numerical Results. *Materials* **2022**, *15*, 910. [CrossRef]
36. Rolph, S. Fractal Geometry: Mathematical Foundations and Applications. *Math. Gaz.* **1990**, *74*, 288–317.
37. Esau, K. *Anatomy of Seed Plants*, 2nd ed.; Wiley: Hoboken, NJ, USA, 1977; Volume 90.
38. Liu, M.; Li, S.; Zhang, K.; Yang, H.; Wang, S. Vortex Structure Analysis of Grooved Surface Flow Loss. In Proceedings of the 2018 4th International Conference on Energy Equipment Science and Engineering (ICEESE 2018), Xi'an, China, 28–30 December 2018; p. 034101.
39. Vigdorovich, I.I. Turbulent thermal boundary layer on a plate. Reynolds analogy and heat transfer law over the entire range of prandtl numbers. *Fluid Dyn.* **2017**, *52*, 631–645. [CrossRef]
40. Reynolds, O. On the Dynamical Theory of Incompressible Viscous Fluids and the Determination of the Criterion. *Philos. Trans. R. Soc. Lond.* **1895**, *186*, 123–164.
41. Blasius, H. Boundary Layers in Liquids with Low Friction. *Z. Math. Phys.* **1908**, *56*, 1–37. (In German)
42. Lee, S.J.; Lee, S.H. Flow field analysis of a turbulent boundary layer over a riblet surface. *Exp. Fluids* **2001**, *30*, 153–166. [CrossRef]
43. Bechert, D.W.; Bruse, M.; Hage, W.V.; Van der Hoeven, J.T.; Hoppe, G. Experiments on drag-reducing surfaces and their optimization with an adjustable geometry. *J. Fluid Mech.* **1997**, *338*, 59–87. [CrossRef]

Disclaimer/Publisher's Note: The statements, opinions and data contained in all publications are solely those of the individual author(s) and contributor(s) and not of MDPI and/or the editor(s). MDPI and/or the editor(s) disclaim responsibility for any injury to people or property resulting from any ideas, methods, instructions or products referred to in the content.